ACS APPLIED MATERIALS & INTERFACES

Research Article

www.acsami.org

Molecular Mobility of Scaffolds' Biopolymers Influences Cell Growth

Rok Podlipec,[†] Selestina Gorgieva,[‡] Darija Jurašin,[§] Iztok Urbančič,[∥] Vanja Kokol,[†,‡] and Janez Štrancar*[,†,∥]

[†]Centre of Excellence NAMASTE, Jamova cesta 39, SI-1000 Ljubljana, Slovenia

[‡]Institute for Engineering Materials and Design, University of Maribor, Maribor SI-2000, Slovenia

[§]Laboratory for synthesis and processes of self-assembling of organic molecules, Ruder Boskovic Institute, Bijenicka 54, Zagreb HR-10000, Croatia

[∥]Laboratory of Biophysics, Jožef Stefan Institute, Jamova cesta 39, Ljubljana SI-1000, Slovenia

Supporting Information

ABSTRACT: Understanding biocompatibility of materials and scaffolds is one of the main challenges in the field of tissue engineering and regeneration. The complex nature of cell−biomaterial interaction requires extensive preclinical functionality testing by studying specific cell responses to different biomaterial properties, from morphology and mechanics to surface characteristics at the molecular level. Despite constant improvements, a more general picture of biocompatibility is still lacking and tailormade scaffolds are not yet available. The scope of our study was thus the investigation of the correlation of fibroblast cell growth on different gelatin scaffolds with their morphological, mechanical as well as surface molecular properties. The latter were thoroughly investigated via polymer molecular mobility studied by site-directed spin labeling and electron paramagnetic resonance spectroscopy (EPR) for the first time. Anisotropy of the rotational motion of the gelatin side chain mobility was identified as the most correlated quantity with cell growth in the first days after adhesion, while weaker correlations were found with scaffold viscoelasticity and no correlations with scaffold morphology. Namely, the scaffolds with highly mobile or unrestricted polymers identified with the cell growth being five times less efficient (N_{cells} = 60 ± 25 mm^{-2}) as compared to cell growth on the scaffolds with considerable part of polymers with the restricted rotational motion (N_{cells} = 290 ± 25 mm^{-2}). This suggests that molecular mobility of scaffold components could play an important role in cell response to medical devices, reflecting a new aspect of the biocompatibility concept.

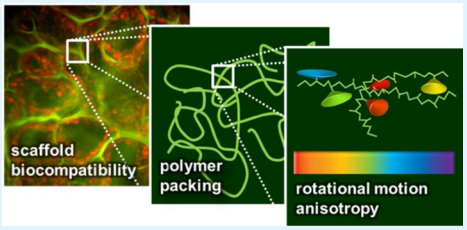

KEYWORDS: *scaffold biocompatibility, polymer mobility, morphology, viscoelasticity, cell growth*

INTRODUCTION

Biomaterial tissue engineering is relatively young research area,[1] investigating complex scaffolds and advanced materials by high-end characterization methods and translating the research from preclinical to clinical phases to meet diverse clinical applications.[2] One of them is scaffold engineering, the rapidly growing multidisciplinary field which incorporates the synthesis of biologically relevant materials and the production design, both essential for the cell−material interface.[3] To achieve an increased scaffold complexity while controling morphology and precisely regulating cell behavior, a computer-aided design approach is frequently implemented.[4,5] Mixing different polymer materials and cross-linking techniques is another currently implemented practice, producing scaffolds with extreme functionalities to meet a variety of applications.[6,7] However, the best approximation of native mechanical and biological properties are obtained by scaffold fabrication through decellularization process of the tissues,[8] where the preserved extracellular matrix (ECM) provides the native compositional and structural environment, crucial for cell recognition and tissue formation, but even with this procedure many significant challenges remain.[9]

The scaffold design currently limits either porosity which can restrict the perfusion. i.e. blood supply into the scaffold once introduced into the tissue,[10] or production time while achieving adequately porous tissue networks.[11] Poorly controlled cell seeding combined with lack of cell infiltration into the structure represent another problem which can reasonably limit successful implementation of a number of scaffold designs, essentially calling for modifications.[12] However, the crucial limitation or more precisely the key issue regarding all scaffold designs is unpredictable biocompatibility, which became even more difficult to understand while the complexity of the scaffolds is increasing.[3]

What makes biocompatibility so elusive is its origin in a complex world of cell−biomaterial interaction.[13,14] Its convoluted nature imposes extensive preclinical functionality testing,[15] that needs to simulate diverse conditions and elucidate not only the "first contact" response but also its time evolution through tissue regeneration and biomaterial

Received: June 13, 2014
Accepted: August 25, 2014
Published: August 25, 2014

degradation,[16] which altogether features the importance of the material and tissue contact duration.[17] With the additional requirement of minimazing the inflammatory response after implantation of biomaterials in the body[18] and the need for their rational cost-effective design,[19] the development is currently focused on mimicking the properties of the native ECM to promote a relevant physiological environment.[20,21]

Such a bionic way has successfully resulted in the composition and functionalization of various scaffold matrices through identification of the essential molecular ECM compounds.[22] Although many aspects of cell–biomaterial interaction have been identified,[23−25] the puzzle of their rational control is still unresolved. Currently, the majority of preclinical biocompatibility testing of scaffolds, composed from variety of synthetic and natural polymers, focuses on cell responses to the substrate, from cell adhesion, proliferation, migration, differentiation, to ECM secretion. The search for crucial parameters modulating such cell responses is organized in three directions (Figure 1): *scaffold morphology* by evaluation

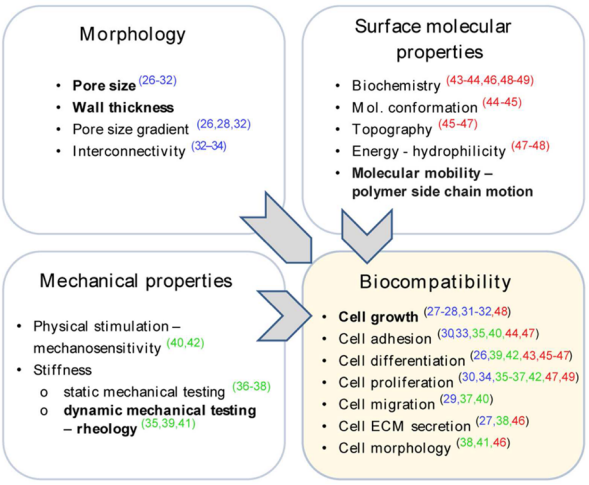

Figure 1. Schematic overview of the scaffold properties investigated to resolve biocompatibility. Traditionally, macroscopic scaffold physical properties such as *morphology* and *mechanical properties* have been investigated, while recently great attention has been dedicated to characterize the influence of *surface molecular properties*, which involves surface biochemistry, molecular conformation, topography, hydrophilicity, etc. In our study, combination of properties with special focus on molecular mobility was studied and correlated with cell growth (bold text) in order to get more insight into the complex nature of biocompatibility.

of the pore size[26−31] and interconnectivity,[32−34] essential for cell promotion and nutrition transport; *scaffold mechanical properties* by evaluation of the influence of stiffness, viscoelasticity and physical stimulation,[35−42] essential for cell focal adhesion, communication, shape and motility as well as material degradation dynamics; and *scaffold properties on the molecular level* by evaluation of the effect of surface chemistry, energy, topography and specificity,[43−49] essential for the cell–scaffold contact.

Despite constant improvements, biocompatibility of particular material with selected cell line or tissue cannot be predicted due to lack of generalized picture of cell response to various materials, precluding the production of tailor-made scaffolds.[50] Traditionally, each scaffold property is correlated by specific cell response in a statistical way or a trial-and-error approach (Figure 1), missing the correlation between different material properties and cell responses and, even more importantly, scattering the investigation focus away from the actual mechanisms of biocompatibility.

The aim of our study was thus the investigation of the influence of scaffold properties on various scales, from molecular to macroscopic, on the cell growth (presented in bold text in Figure 1). Motional analysis of the scaffold polymers, which presents the molecular characterization, was employed for the first time in scaffold biocompatibility research, where it has only been noted as being of potential relevance.[51]

EXPERIMENTAL SECTION

Chemicals and Materials. Gelatin type B (Sigma-Aldrich, St. Louis, MO) derived from lime cured bovine skin with isoelectric point (pI) of 4.7−5.2, bloom number of 225 and the average molecular weight of 47 kDa was used as a scaffold material. 0.1 M phosphate and carbonate buffers were used as a scaffold solutions and were prepared from sodium phosphate monobasic dihydrate, sodium phosphate dibasic heptahydrate, sodium carbonate, and sodium bicarbonate, all purchased from Sigma-Aldrich (Steinheim, Germany). 1-Ethyl-3(3-(dimethylamino)propyl)-1-carbodiimide hydrochloride (EDC; Carbosynth, Compton, UK) and *N*-hydroxysuccinimide (NHS; Sigma-Aldrich, Steinheim, Germany) were used to cross-link gelatin amino-acids during the scaffold preparation. Fluorescein isothiocyanate isomer I (FITC; Invitrogen, Eugene, Oregon) and 3-maleimido PROXYL (Sigma-Aldrich, Steinheim, Germany) were further used as a fluorescent and spin probes to label the side chains of gelatin polymers, respectively. L929 mouse fibroblasts were purchased from tissue engineering company Educell d.o.o. (Ljubljana, Slovenia) and the fatty acid fluorescent probe SPP158 (Figure S5 in the Supporting Information), synthesized at the Faculty of Pharmacy (University of Ljubljana, Slovenia), was used to label the cell membrane.

Scaffold Preparation. Scaffolds were prepared with 10% (w/v) gelatin solution at different pH (pH 7.5 phosphate buffer and pH 9.5 carbonate–bicarbonate buffer). The solutions were first let to swell under gentle stirring at room temperature and then heated up to the temperature of 50 °C to overcome macroscopic gel–sol or microscopic helix–coil transition to completely suppress gelatin chain helicity,[52] enabling more efficient cross-linking and labeling by increasing accessibility of the (primarily) lysine sites. Randomly coiled gelatin polymers were then successfully functionalized by site-directed labeling mainly toward primary amine groups for further scaffold analysis. Fluorescent probe FITC (reactive via isothiocynate group[53]) and spin probe 3-maleimido PROXYL (reactive via maleimido group[54]) were used in a molar ratio of 1:2000 to the predetermined number of the available free amino groups, with more than 95% of ε-amines and less than 5% of α-amines, the number estimated by lysine concentration and the average molecular weight of gelatin chains. Labeling of cysteines, with approximately 1 order of magnitude faster reaction at solution pH of 7.5 (higher percentage of unprotonated groups) and at least 2 orders of magnitude lower molar ratio, can contribute to minor electron paramagnetic resonance (EPR) signal—the major contribution still being assigned to labeling of lysines. Meanwhile, at solution pH of 9.5, cysteine labeling is negligible and does not contribute to any EPR signal, since the reaction is much more efficient on lysines due to amine group nucleophilicity. The chosen molar ratio enabled good detection of FITC fluorescent signal by fluorescence microscopy as well as good signal-to-noise ratio (S/N) of acquired EPR spectra, while keeping the sample practically unchanged due to low percentage of labeled chains. Cross-linking of gelatin polymers was done by water-soluble EDC and NHS (molar ratio of 4:1) to produce stable amide bonds, where the molar concentration of EDC with respect to the number of gelatin free carboxylic groups was 1:1 and 0.15:1. Also other cross-linking techniques, such as enzymatic with tyrosinase and transglutaminase-mediated cross-linking, genipin, and phenolic acid based cross-linking had been employed, but did not yield scaffolds which would be as stable and porous as in the case of

EDC/NHS. To control cross-linking process by temperature regulation, the cross-linkers were mixed with the gelatin solution into Teflon Petri dishes (d = 50 mm) placed at the temperature-controlled plate just prior freezing-thawing process to apply the so-called cryogelation.[7,55] Thawing cycle was performed between −10 and 0 °C in the time interval of 10 h. The formed ice-templated, porous scaffolds were dialyzed against the appropriate buffer to remove the excess of nonreacted cross-linkers and labeling probes. Samples were then stored at T = 6 °C until further sterilization and analysis. By using different pH and cross-linker concentration throughout the preparation, different properties of scaffolds were obtained for further investigation (Table 1). To simplify terminology, the scaffolds will be designated as scaffold **1**−**4**.

Table 1. Preparation Parameters of Investigated Scaffolds

samples	buffer pH	n (EDC): n (free COOH sites)[a]
scaffold **1**	9.5	0.15
scaffold **2**	9.5	1
scaffold **3**	7.5	0.15
scaffold **4**	7.5	1

[a]Molar ratio.

Scaffold Sterilization. Samples were cut into thin pieces of the dimensions of approximately 30 mm × 5 mm × 5 mm, immersed in a 70% ethanol solution for 2 h (V = 50 mL) and then exposed to UV irradiation in a sterile atmosphere for 30 min. Samples were dialyzed three times with sterile PBS (V = 50 mL, buffer changed each day) and stored at 6 °C for further cell growth experiments.

Polymer Side Chain Mobility Analysis by EPR Spectroscopy. Site-directed spin labeling (SDSL) with 3-maleimide PROXYL on the gelatin primary amines and on traces of cysteine thiol groups was performed before scaffold preparation to elucidate the side chain conformational dynamics of polymers through EPR spectral line shape analysis, as described before.[56,57] Since spin probe size is similar to that of the protein side chain and much smaller than polymer itself, there is no significant influence of the probe on the polymer motion. Consequently, spin probe rotational motion basically reflects available space for side chain wobbling which is in addition superimposed on the polymer motion. If protein/polymer backbone is folded then backbone motion is slow and the anisotropy of the spin probe fast conformational motion characterizes the packing of the local protein side chains. These principally depend on the protein secondary structure and packing of the several proteins together (fibers, bundles, networks, etc.). In such a case the probe motion is fast, restricted and thus anisotropic. On the other hand, when protein backbone is unfolded (i.e., random coil), its reorientational motion is faster and, more important, much less restricted, significantly increasing the space available for spin probe to wobble. In this case the probe motion is fast, unrestricted and thus almost isotropic. The anisotropy of the spin probe conformational motion can therefore be a good indicator for local polymer mobility, as schematically presented in Figure 2a.

For the analysis, samples were put into quartz capillary tubes of diameter of 1 mm and transferred into the temperature-controlled EPR resonator. EPR measurements were done on X-Band Bruker Elexsys E500 Spectrometer (Karlsruhe, Germany), with microwave frequency of 9.3 GHz, the power of 20 mW, modulation frequency of 100 kHz and field modulation amplitude of 0.2 mT. Several spectra were accumulated to obtain the signal-to-noise ratio (S/N) of 200−300, suitable for further spectral simulation and analysis. Temperature-dependent polymer mobility measurements were performed in cooling−heating cycles from room temperature down to 5 °C, followed by a temperature ramp-up to 80 °C in steps of 15 °C, and a final decrease down to room temperature to check for reversibility or potential temperature-induced structural changes.

Spectral analysis took into account that local polymer rotational motion varies from fast unrestricted at unfolded ends and unstructured parts of gelatin polymer chains to fast restricted motion within structured and densely packed parts of chains, both motional patterns being sensitive to temperature. The impact of the anisotropy and rate of reorientational motion of the spin label attached to a polymer on the EPR spectral line shape was employed to detect molecular motion[57] measured at different temperature. The gray bands indicated in Figure 2b show the spectral regions where the line shape can reflect the motional anisotropy. To extract the information in these parts, we needed to employ spectral simulations to decouple a sharp-triplet component -3 equal hyperfine lines, reflecting part of the labels being motionally unrestricted - from a component arising from fast tumbling but sterically restricted labels. Spectrum of a disordered polymers in solution (Figure 2c), is on the other hand composed of only one spectral component with the sharp triplet due to its isotropic wobbling. By the mentioned spectral simulations done within the software EPRSIM-C (http://lbf.ijs.si/download.html),[58] the anisotropy of the restricted rotational motion was revealed and described by *free rotational space* Ω, defined as $\Omega = \theta\varphi/(2\pi)^2$, where θ and φ are the two cone angles of restricted rotational motion.[59,60] The free rotational space analysis through the entire temperature region was used to characterize the phase transitions of a polymer structure through the detection of phase transition temperature ($T_{ph.tr.}$), dependent on molecular packing and intramolecular interactions.[61] Additionally, average free rotational space Ω_{AVG} was calculated at the temperature T = 37 °C as $\Omega_{AVG} = \sum_i d_i\Omega_i$ to characterize an average polymer mobility at the spin labeled amines. Ω_i presents the free rotational space of the corresponding spectral component, and d_i, its weight.

Morphology Characterization by Confocal Fluorescence Microscopy (CFM). For this purpose, primary amine groups, mainly on lysine side-chains of polymers, were covalently labeled with reactive isothiocyanate group of FITC fluorescent probe before scaffold

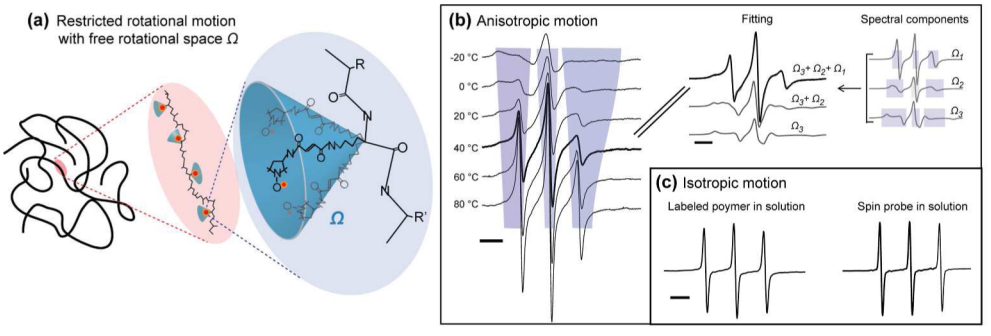

Figure 2. Temperature dependent spectral analysis of polymer mobility. (a) Schematic view of site-directed spin labeling and its conformational dynamics characterized by cone wobbling model. (b) Spectra of anisotropic wobbling of polymers in scaffold matrix composed of several spectral components. Temperature induced polymer structure changes influence the anisotropy and the rate of reorientational motion reflected in the line shape indicated within gray bands. (c) Spectra of isotropic wobbling, of polymers in solution (left) and free spin probe in solution (right). Spectra have a sharp triplet with narrow spectral lines. The bar range is 10 G.

preparation. Scaffolds were cut to fit into a Nunc Lab-Tek chambered coverglass (Thermo Scientific, Denmark) and placed onto the inverted microscope Nikon Eclipse TE 2000-E. Images were acquired under 15× objective magnification in confocal mode with Lambda LS xenon-arc lamp source (Sutter Instrument, Novato, USA) and iXon EMCCD camera (Andor, Ireland). For optimal fluorescence detection, excitation, dichroic and emission filters of the CARV II unit (BD Biosciences, Franklin Lakes, USA) were selected to meet FITC absorption/emission spectra.

Acquired images of the optical cross sections were then analyzed to characterize wall thickness and pore size distributions using several 1D intensity profiles across an image (Figure 3a). Efficient fluorescent

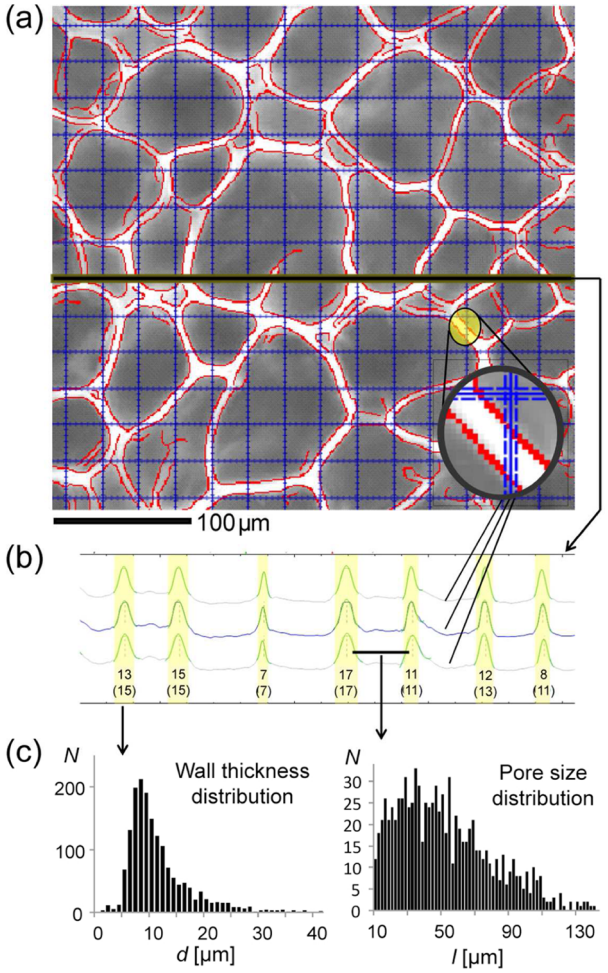

Figure 3. Scaffold wall thickness and pore size analysis. (a) Scaffold walls were located by computer designed surface detection based on intensity differences in the acquired fluorescence microscopy image (thin curves surrounding the walls). (b) Line intensity profiles of horizontal/vertical slices were extracted from an image, and the walls' signals (shaded regions) were used to fit the wall thickness via modified Gaussian curves. Calculated values in micrometers are presented in the bottom, where they were additionally corrected due to the walls' and the line profile intersection angle. (c) The wall thickness and the pore size distributions presented with histograms.

labeling, resulting in a good contrast of fluorescence intensity between scaffold walls and pores, enabled accurate positioning of the scaffold wall boundaries (Figure 3a) and wall intensity profiles (Figure 3b), which were fitted with modified Gaussian curves (shaded regions) to determine wall thickness at each position detected (the values at the bottom in μm). To correct the obtained wall thicknesses for nonperpendicular crossings of the walls with the line profile, the crossing angles were calculated from the shifts of the wall positions at two reference line profiles in direct vicinity to the primary one (Figure 3a, inset). Analyzing several line profiles across 5−10 images of the same sample at different sites, sufficient statistics was obtained for construction of the wall thickness distribution histogram (Figure 3c). The same intensity profiles were used also to calculate the pore size distribution, where the distance between two closest walls was used to estimate the pore diameter. The average wall thickness and pore size with their standard deviations were finally calculated from acquired and analyzed images (5−10 for each sample). Several images of morphology with the corresponding analysis comprehended in histograms are shown in Figures S2 and S3 in the Supporting Information.

Mechanical Characterization by Rheology. Dynamic shear oscillation measurements at small strain were performed to characterize the rheological properties of the fabricated scaffolds. This was carried out at HAAKE RT20 Rotovisco-Oscillatory Rheometer (Thermo Scientific, Germany) in parallel plates oscillatory mode, with 30 mm plate diameter and gap distance adjusted to scaffold thickness. Mechanical spectra were recorded in a constant strain mode over the frequency range of 0.1−100 rad/s in linear viscoelastic region (LVE) with the sample deformation of 0.01%, predetermined with amplitude sweep measurement. Variations in storage (G') and loss modulus (G'') were recorded at 37 °C.

In case of classical viscoelastics (spring−dashpot Maxwell viscoelastic model) the log−log presentation of loss modulus (G'') shows a clear maximum at an eigenfrequency ω_0 and a linear decrease at higher frequencies, none of which were observed from experimental data (Figure 8, insets). Maxwell model was thus modified with the linear combination of spring-dashpot modes (Figure 4) (G_i' gray

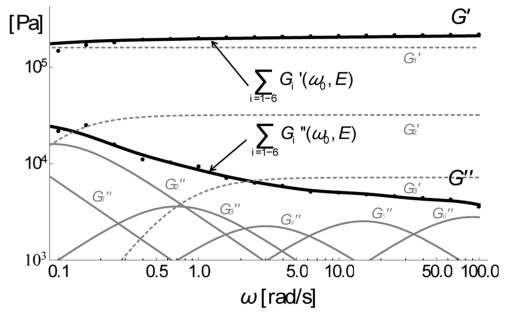

Figure 4. Rheological characterization of scaffolds. The measured frequency dependent storage (G') and loss (G'') moduli (black points) were fitted with generalized Maxwell model as a linear combination of six spring-dashpot modes (G_i' gray curves; G_i'' gray dashed curves; last three not in range). Each mode was characterized by its eigenfrequency $\omega_{0,i}$ and corresponding elastic modulus E_i.

dashed curves, G_i'' gray curves), each characterized by its eigenfrequency $\omega_{0,i}$ and corresponding elastic modulus E_i—an analogue of the n-parameter model presented in ref 62. In terms of scaffold structural or physical properties, $\omega_{0,i}$ can be interpreted as a quantitative value defining a particular pore type in the scaffold network, while the corresponding E_i as a value describing the stiffness of the pore wall. For example, smaller pores undulate with higher eigenfrequencies and thus take over the stress at higher frequencies, while bigger pores deform more at lower frequencies. On the other hand, thicker pore walls at the constant cross-linking density possess higher stiffness and can thus sustain more load in comparison with thinner pore walls. Since the elastic moduli decreased at higher frequencies, the scaffold became less stiff at higher frequencies, i.e. could sustain less load as compared to lower frequencies. Smaller pores can naturally sustain higher ω_0 before significant deformation, while thicker pore walls correspond to higher E and can thus sustain more load.

At least six spring−dashpot modes were required to fit the frequency dependence of the scaffolds moduli. Pairs of the fitted $\omega_{0,i}$ and E_i are presented graphically in Figure 8 and interpreted as a

dx.doi.org/10.1021/am5037719 | ACS Appl. Mater. Interfaces 2014, 6, 15980−15990

mechanical spectrum of the scaffold. The complexity of the scaffold viscoelasticity comes from its structural inhomogeneity due to broad pore size and wall thickness distribution across its profile.

Cell Growth. L929 fibroblasts were used for cell growth studies on gelatin scaffolds. Since our objective was to study spreading and growth of the cells across fabricated, cartilage targeted scaffolds with large porosity, imitating such tissues, this particular type of cells was intentionally chosen as they fill spaces and form ECM components within connective tissues throughout the body including cartilage.

Scaffolds were cut into a small slices (5 mm × 3 mm × 3 mm) and put for 1 h in a cell growth medium (DMEM supplemented with Fetal Bovine Serum) at 37 °C before cell culturing. Scaffolds were transported into Nunc Lab-Tek chambered coverglass and seeded with 400 μL of cell suspension (10^5 cells/mL), gently poured over the scaffold in three parallels. Seeded scaffolds were incubated at 37 °C in 5% CO_2 atmosphere for 2 days. Cell growth was measured with CFM using fatty-acid membrane fluorescent probe SPP158 with Rhodamine B attached to the polar head (Figure S5 in the Supporting Information). Briefly, 2 μL of 10^{-4} M of probe diluted in ethanol was mixed with 400 μL of the DMEM medium, which was used to stain the cell membranes for 5 min. Samples were gently rinsed with sterile PBS before measurements to remove all excess fluorescent probe. Images were taken under 15× magnification.

Cell number was analyzed via thresholding the cell intensity against the darker environment (Figure 5b). The cell density (N_{cells}/unit^3) was obtained by dividing cell surface area (red region, Figure 5c) with the average surface of a single cell estimated prior the analysis. More valuable representation of cell density was acquired by normalization of the cell number to the scaffold surface available for cell growth (N_{cells}/unit^2). Since the latter depends mainly on the pore size (within the thin confocal volume), cell density was simply normalized to an average pore size derived from morphology analysis as described previously.

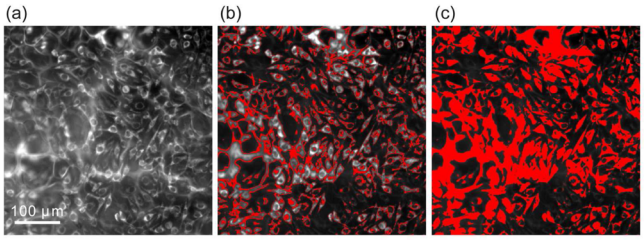

Figure 5. Cell growth characterization. (A) Original CFM image acquired under 15× magnification; (b) detection of cell boundaries by thresholding image intensity; and (c) surface area of cells in a confocal optical volume. Average number and its standard deviation were calculated from 5 to 10 acquired images.

RESULTS

Molecular Mobility of Polymer Side Chains. The scaffolds were first analyzed in terms of polymer mobility using spin labeling EPR spectroscopy (as described in the Experimental Section), characterizing the polymer side chain rotational motion anisotropy via space angle (cone), where the side chain is allowed to wobble unrestricted. The revealed temperature-dependent motional restrictions of the spin labeled polymer side chains are presented in Figure 6 with "bubbles", where each bubble represents one detected motional pattern characterized with the free rotational space Ω_i related to the anisotropy of rotational motion (y axis) and the size corresponding to the relative weight d_i of the corresponding motional pattern (the exact values are presented in Table S1 in the Supporting Information). The results in Figure 6 are sorted by the measured phase transition temperature ($T_{ph.tr.}$) at which anisotropic motional component disappeared. All other results in the paper are presented in the same sequence to foster detection of the potential correlations. $T_{ph.tr.}$ represents measurable physical quantity which reflects the temperature at which tight packing of polymers is lost resulting in a sudden change from anisotropic-to-almost-isotropic conformational motion of spin probe caused by structural changes of a polymer network. Note that conformational entropy of polymer chains become dominant in the free energy above this transition and the conformational space of a polymer chains is maximized. This of course does not mean that the number of cross-linking sites changes during such a transition.

In the measured temperature range from 0 to 70 °C, $T_{ph.tr.}$ for scaffolds **1**−**4** was detected at around 0 °C, between 25−35, 40−50, and 55−60 °C, respectively (Figure 6, red dotted bands). Regarding the coexistence of different motional patterns through the temperature range scanned, scaffold **1** exhibited nearly isotropic local polymer motion without any other restricted motion through the entire range as represented by the dominating motional pattern with high free rotational space Ω. On the other hand, the rest scaffolds were identified through the coexisting isotropic and anisotropic motional patterns with the weight of the restricted motional component increasing from scaffolds **2** to **4**. The EPR spectra acquired at T = 37 °C are shown above the temperature diagrams, where the

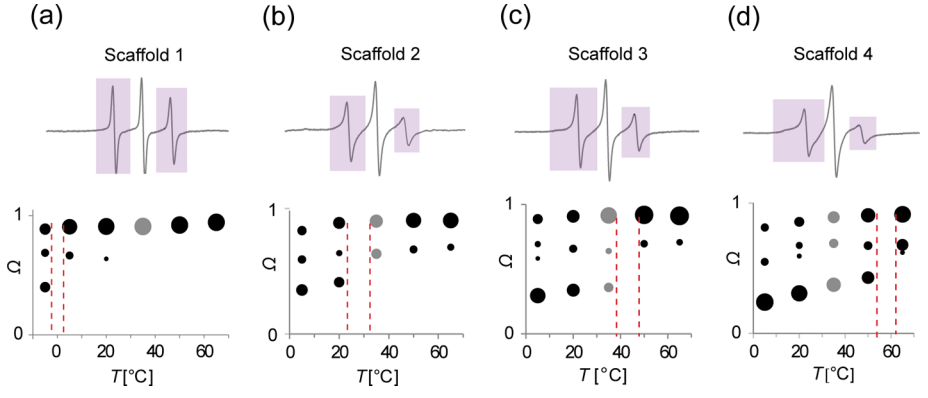

Figure 6. Temperature dependent gelatin polymer mobility via free rotational space Ω analysis for scaffolds **1**−**4** designated with (a−d). The fitted spectral components characterized with Ω are presented with bubbles with the size proportional to their weight. EPR spectra acquired at 37 °C are shown above with indicated the most sensitive parts to the changes in the molecular mobility. Red dotted bands represent the temperature region of polymer mobility $T_{ph.tr.}$

dx.doi.org/10.1021/am5037719 | ACS Appl. Mater. Interfaces 2014, 6, 15980−15990

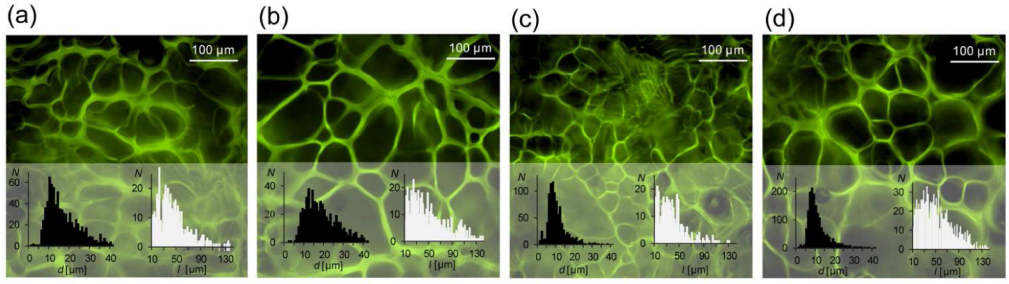

Figure 7. Morphology of scaffolds **1**–**4** (a–d) with wall thickness (black) and pore size (white) distributions in the insets. Different pH values and cross-linker EDC/NHS concentrations were used to induce morphology variation. Images of fluorescently labeled scaffolds were acquired with CFM under 15× magnification.

main spectral differences were observed in the two side absorption peaks, most sensitive to the anisotropy of the rotational motion (indicated within colored bands). The other spectra acquired in the whole temperature can be seen in Figure S1 in the Supporting Information.

Scaffold Morphology. Morphology of the porous gelatin scaffolds was studied by confocal fluorescence microscopy (CFM) by obtaining typical optical cross sections as shown in Figure 7. CFM images revealed well-defined walls and interconnected pores resulting from simultaneous freezing and cross-linking process during scaffold preparation. The scaffolds' wall thickness (d) and pore size distributions (l) were analyzed in terms of histograms as shown in Figure 7 insets, marked in black and white color, respectively. The scaffolds' wall thicknesses were $d_1 = 17.1 \pm 0.7$ μm, $d_2 = 19.2 \pm 0.5$ μm, $d_3 = 10.1 \pm 0.6$ μm, and $d_4 = 11 \pm 2$ μm, with an error representing standard deviation of the average values of distributions acquired from 5 to 7 analyzed images. Wall thickness was almost two times smaller in the scaffolds 3 and 4 (Figure 7c and d), which is, considering the scaffold preparation, a consequence of the pH used. It should be stressed that the correlation between the wall thickness and pH reflects the importance of a polymer net charge during scaffold structure formation throughout cryogelation. Namely, the latter depends on dissociation of carboxylic groups and protonation of amino groups. In the applied pH range primarily protonation of amine groups changed, modifying polymer net charge. With the latter being modulated and the amount of polymer being constant in all scaffolds, the wall thickness variation actually reflects the polymer packing. On the contrary, no correlation between the wall thickness and the concentration of the cross-linkers was observed.

The pore size average values of $l_1 = 45 \pm 3.5$ μm, $l_2 = 52 \pm 6$ μm, $l_3 = 38 \pm 3$ μm, and $l_4 = 52 \pm 5.5$ μm suggest that they are primarily influenced by the cross-linker concentration and not the pH. Namely, scaffolds with bigger average pore size were prepared at higher cross-linker concentration. Since the influence of the scaffold preparation parameters on its morphological properties was not the main scope of this work, we did not investigate them in more details.

Scaffold Mechanical Properties. Mechanical properties of the scaffolds were determined by rheological measurements (Figure 8) and possible correlations with their morphology were searched for. Storage (G') and loss (G'') viscoelastic moduli (Figure 8, insets) presented with the black and gray curve respectively were characterized at physiological temperature $T = 37$ °C in the frequency range from 0.1 to 100 rad/s. The moduli showed viscoelastic response analogous to Maxwell[56] with nearly constant storage modulus and decreasing loss modulus at higher frequencies, characteristic for elastic material. Comparing the moduli of the measured scaffolds, they differed substantially with respect to their absolute ranges, meaning that such scaffolds would respond in a very different way to stress and handling.

A closer look at the loss modulus curves revealed multiple peaks in the low frequency range and no linear decrease at high frequencies as expected for classical Maxwell viscoelastics, indicating that the complexity of the system exceeded a simple Maxwell model. Scaffold mechanical properties were thus described by a superposition of Maxwell viscoelastic modes as described in the Experimental Section, providing a set of pairs of fitted eigenfrequencies $\omega_{0,i}$ (related to $\tau = 1/\omega_0$, representing stress relaxation time of the material[63]) and corresponding elastic moduli E_i. These sets of pairs are plotted in diagrams in Figure 8. Each of the points can be interpreted to describe Maxwell viscoelasticity of a particular domain type in morphologically complex scaffold structure already revealed by the pore size and the wall thickness distribution. A straightforward analogy is the mechanical spectrum of a truss bridge where differently sized supporting elements damp various frequencies. The dimensions of supporting elements are analogous to pore sizes and wall thicknesses in scaffolds.

The results show higher elastic moduli in scaffolds **2** and **4** (Figure 8b and d), which were prepared with higher cross-linker concentration and vice versa. That indicates the importance of this parameter in final mechanical properties of scaffolds. However, the elastic moduli were not found to fully correlate with the morphological properties since the scaffold with the lowest moduli (Figure 8a) exhibited neither extreme pore sizes nor extreme wall thicknesses indicating that morphological properties do not uniquely determine the mechanical properties. Moreover, the scaffolds with the similar average wall thickness of 17.1 ± 0.7 and 19.2 ± 0.5 μm, shown in Figure 7a and b, respectively, display very different mechanical properties as shown in Figures 8a and 8b, respectively. This originates in the physicochemical properties of the scaffold walls themselves, which are defined by the density of gelatin packing and its cross-linking during preparation. Although this relationship is far from being simple, we can assume that the position and cross-linking degree depend on time evolution of local concentrations of gelatin and cross-linkers. The latter are concentrated by the surrounding freezing nuclei, where the rate of freezing (i.e., concentrating) and cross-linking are temperature-dependent. Variable time evolution of all the concentrations therefore implies also variable mechanical properties of the material.

As an example, scaffold **1** was engineered with the lowest amount of cross-linkers at high pH, which influenced the

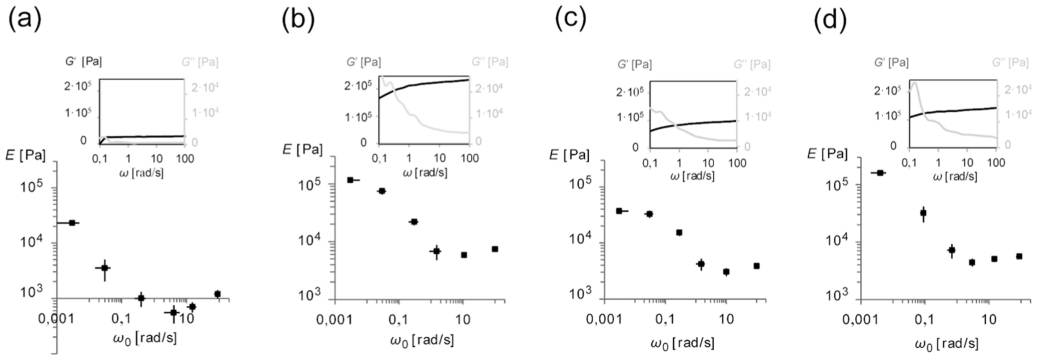

Figure 8. Mechanical properties of scaffolds **1**−**4** (a−d) with pairs of fitted eigenfrequencies $\omega_{0,i}$ and corresponding elastic moduli E_i (black dots) of the generalized Maxwell model. Raw data of G' and G'' is presented in the insets.

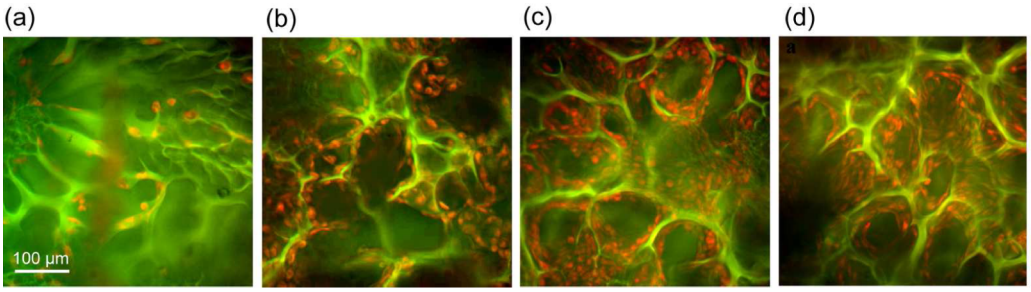

Figure 9. Cell growth on scaffolds **1**−**4** (a−d) measured after 2 days of culture. Cells (red) and scaffolds (green) were labeled with Rhodamine B membrane probe and FITC respectively. Images were acquired under 15× magnification with CFM using two sets of pairs of light excitation and emission filters, corresponding to the fluorescence characteristic of each probe.

protonation of the targets involved in cross-linking. Such a procedure resulted in least cross-linked matrix and loose packing as seen through almost two-times higher wall thickness and in the lowest elastic moduli (Figure 8a).

Cell Growth. To investigate the influence of scaffolds' molecular, morphological and mechanical properties (Figures 6−8) on its biocompatibility, growth of L929 fibroblasts was monitored after 2 days of culture (Figure 9). By using two sets of fluorescence detection filters, CFM images nicely show cell population with respect to the scaffold structure. Noticeable differences were identified between the group of scaffolds **2**−**4** (Figure 9b−d) and scaffold **1** (Figure 9a), with the approximately five times lower cell growth. First, the number of cells per unit volume (N_{cells}/mm^3) obtained directly from an acquired CFM images was determined: N_1 = 9000 ± 3000, N_2 = 31000 ± 8000, N_3 = 46000 ± 4000, and N_4 = 32000 ± 4500. Second, the number of cells per scaffold surface available for cell growth (N_{cells}/mm^2) was calculated by normalization with their average pore sizes: N_1 = 60 ± 25, N_2 = 270 ± 70, N_3 = 290 ± 25, and N_4 = 280 ± 40. The 5−10 cross sections were selected from total 3 scaffolds with at least one cross-section from each scaffold. More than two were selected from those scaffolds that were less homogeneously populated. An error represents standard deviation of the average cell growth obtained from three scaffold parallels. For more cell growth images see Figure S4 in the Supporting Information.

Cell growth was measured also after 1 week of culture using CFM as well as Resazurin cell viability assay. As the cells started to crowd, i.e. densely populating the scaffold, the precise evaluation of the growth was not possible. The measurements of Resazurin fluorescence felt out from the linear regime of fluorescence intensity-cell number dependency of the viability test.[64] Nevertheless, it seems that cell growth differences between the scaffold decreased with time indicating that the cells slowly adapt even to the less appropriate scaffolds, very likely by producing their own matrix elements which are incorporated in the local microenvironment and thus masking the material native properties, including the mobility of a polymer network.

DISCUSSION

In scaffold research, *dynamics* is usually associated with cell proliferation.[65] Some studies connect it also to the scaffold degradation rate[65] and ECM deposition,[24] where the relative motion of cells depends on disintegration of the matrix as well. Since scaffolds can also be exposed to mechanical stress during their application, dynamics sometimes refers also to material compression vibration and consequent cell response.[42] However, all these perspectives neglect dynamics on smaller, submicron scales. Our study therefore extended the exploration to the molecular scale, focusing on correlations between the polymer molecular dynamics and the cell growth, morphology, and mechanical properties.

Different scaffolds, composed of a natural biocompatible and biodegradable polymer, gelatin type B, were fabricated at different pH and concentration of EDC/NHS cross-linkers. Without an intention to investigate the chemistry or the efficacy of the cross-linking of the scaffolds, the variation of these parameters was implemented only to obtain a set of scaffolds with different properties to search for correlations with cell growth (Figure 10). Best correlation was shown with scaffold molecular mobility, specifically with the polymer dynamics phase transition temperature $T_{ph.tr.}$, (R^2 = 0.92), while no significant correlation was observed with morphology and partial correlation was identified with mechanical properties (R^2 = 0.45), with significantly suppressed growth evidently below a

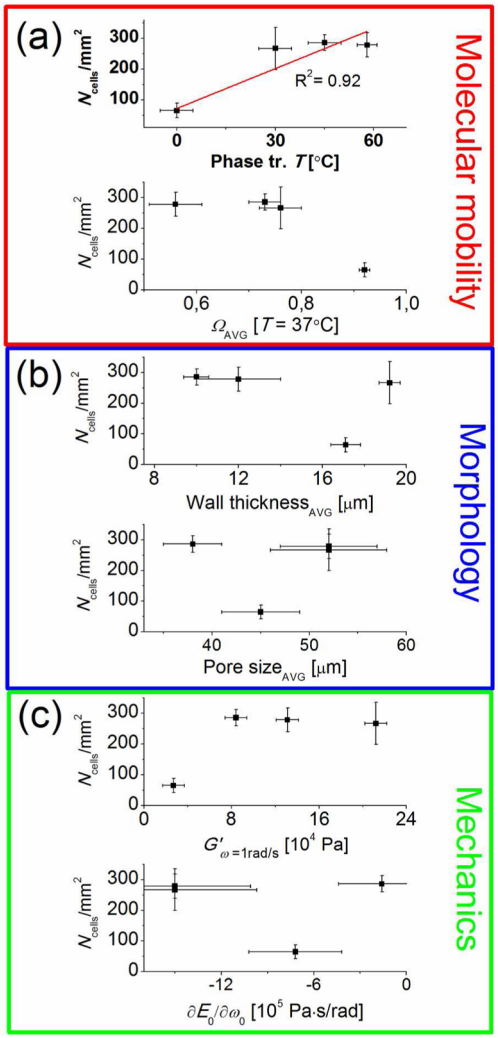

Figure 10. Search for the best correlation between cell growth presented as cell surface density and scaffold properties on (a) *molecular scale* (polymer mobility phase transition temperature and average free rotational space), (b) *microscopic scale* (average wall thickness and pore size), and (c) *macroscopic scale* (storage modulus and elasticity dynamics of generalized Maxwell model). The errors on *y*-axis are standard deviation of the average cell growth obtained from three scaffold parallels and the errors on *x*-axis standard deviation of (a) 3, (b) 5−10, and (c) 3 measurements.

threshold value of the storage modulus G'. Here we discuss the results more systematically.

Over the last years, great attention in the research field of tissue engineering has been paid to the investigation of the effect of scaffold nanostructures on cell responses at various levels. It has been shown that tuning the scaffold structure at the molecular level by modification of the surface chemistry and topology affects cell differentiation,[43−45] alter molecular conformation of surface bound peptides responsible for cell adhesion,[43] modify the surface organization during cell ECM secretion,[46] etc. (Figure 1). Even surface molecular mobility has been noticed once to impact cell response,[51] but never investigated thoroughly. Our study was thus focused on the investigation of the molecular mobility of scaffold polymer (side) chains by spin labeling EPR spectroscopy. For that purpose, gelatin polymers were specifically labeled with 3-maleimide PROXYL spin label, attached to the primary amine groups of lysines and the potential thiol groups of cysteines during scaffold preparation,[54] resulting in an uniform distribution of probes across the scaffold and a complex EPR spectra (Figure 6). The spectral simulations were used to extract temperature dependent coexisting motional patterns, presented on the main graphs. Good correlation between cell growth and polymer mobility described with the motional pattern phase transition temperature $T_{ph.tr.}$ was observed (Figure 10a, top). Materials with higher $T_{ph.tr.}$ promote cell growth, where the current experimental accuracy suggests overall dependency as a linear one (with the coefficient of determination to be R^2 = 0.92). However, the data does not exclude the possibility that there exists a threshold value of scaffold $T_{ph.tr.}$ (between 0 and 30 °C), above which cell growth would not depend on polymer mobility dynamics anymore. Note that $T_{ph.tr.}$ is a thermodynamic property of a scaffold polymer network used to characterize the samples, while the cell response reflects directly the polymer mobility itself. Inefficient cell attachment and proliferation during the first days of culture (Figure 9a) is most likely associated with almost completely nonrestricted motion of polymers with the highest free rotational space Ω_{avg} and lowest $T_{ph.tr.}$ (Figure 6a). From the results we can assume that cell growth is promoted if the appropriate part of polymer side chain motion is substantially restricted, characterized with the lowest values of free rotational space Ω (Figure 6, gray bubbles). The correlation is presented in Figure 10a bottom, where the decrease of Ω_{avg} corresponds to the degree of polymer restricted motion, and where the dependency shows the significance of such motional component. The explanation could be found in the cell attachment properties related to the mobility of polymer side chains, where it is believed that the mobility related interaction time for which a polymer binding motif is available for cells to interact with plays a significant role.

In several studies it was emphasized that cell response, involving cell attachment, proliferation, migration and differentiation, critically depends on the scaffold pore size distribution,[27,29,32,33] with different cells having different optimal pore size ranges[28] and that subtle changes of the pore sizes significantly affect the cellular activity.[30] In contrast, some studies reported no effect of the pore size on cell growth.[32] These opposing results question the unique importance of the pore size. Our study cannot reliably confirm that scaffold morphology and cell growth would be either correlated or uncorrelated (Figure 10b). However, the average wall thickness as well as the pore size seemed to be mostly uncorrelated with cell growth.

Going beyond the morphology, correlation with the scaffold mechanical properties was also analyzed. The importance of mechanical properties of the scaffolds on cell adhesion and proliferation has been investigated in numerous studies. Promotion of cellular activity and cell migration was found to be dependent on material stiffness;[35,36] besides, effect of the material stiffness has been identified on the actin cytoskeleton organization and phenotype behavior,[37] as well as on the cell-generated forces and gene expression.[67] In our study, scaffold mechanics (viscoelasticity) correlated with cell growth more than the morphology but on the other hand less than the polymer mobility (Figure 10c). Regarding the storage modulus (G') measured at ω = 1 rad/s, cell growth did not change significantly above G' > 80 kPa and was shown to be much lower at G' < 50 kPa. This could mean that a certain mechanical strength or more exactly a threshold value has to be

reached for efficient cell growth, where additional material strength does not have any significant influence. We believe, however, that cell response might not be directly associated with the mechanical properties on macro-scale. For example, mechanical properties such as eigenfrequencies and related moduli depend on pore size, wall thickness, density of cross-linking and packing of polymers. On the other hand, molecular mobility, which correlated with cell growth to the highest extent, is influenced only by the density of cross-linking and packing of the polymers. Since pore size and wall thickness did not influence on cell growth significantly, but affected on mechanical properties, the latter cannot fully correlate with cell growth. However, G' might not be the best representative of mechanics of such a complex porous material. Instead, the mechanical spectrum in terms of elastic moduli (E_i) vs eigenfrequency ($\omega_{0,i}$) dependence could better represent the scaffold's viscoelasticity (Figure 10c, bottom). Assuming of that and of its correlation with cell growth, polymer molecular mobility was found to be the best indicator of cell growth during the first days of culture.

CONCLUSION

By correlating fibroblast cell growth on gelatin scaffolds with their molecular dynamics studied via spin label EPR spectroscopy, morphology studied via confocal fluorescence microscopy and viscoelasticity studied via rheometry, the molecular mobility was identified to be the most relevant property to indicate cell growth. We believe that the biocompatibility of materials should therefore be characterized with their molecular dynamic properties as well, influencing the cell−scaffold interaction.

ASSOCIATED CONTENT

Supporting Information

EPR spectra of polymer mobility, fitted spectral parameters of polymer motional patterns, CFM images of scaffold morphology, histograms of scaffold pore size and wall thickness distributions, CFM images of cell growth, and chemical structure of membrane fluorescent probe. This material is available free of charge via the Internet at http://pubs.acs.org.

AUTHOR INFORMATION

Corresponding Author

*E-mail: janez.strancar@ijs.si. Tel.: +386 (01) 477 3226. Fax: +386 (01) 477 3191.

Notes

The authors declare no competing financial interest.

ACKNOWLEDGMENTS

This research was financially supported by Centre of Excellence NAMASTE (European Regional Development Fund), Slovenian Research Agency (ARRS) (program P1-0060 and PhD grant no. 1000-09-3), and Gaining Experience Grant from Unity Through Knowledge Fund. We gratefully thank S. Pajk (Faculty of Pharmacy, University of Ljubljana) for synthesizing membrane targeted fluorescent probes.

REFERENCES

(1) Langer, R.; Vacanti, J. P. Tissue Engineering. *Science* **1993**, *260*, 920−926.
(2) Harrison, R. H.; St-Pierre, J. P.; Stevens, M. M. Tissue Engineering and Regenerative Medicine: A Year in Review. *Tissue Eng., Part B* **2014**, *20*, 1−14.
(3) Owen, S. C.; Shoichet, M. S. Design of Three-Dimensional Biomimetic Scaffolds. *J. Biomed. Mater. Res., Part A* **2010**, *15*, 1321−1331.
(4) Gauvin, R.; Chen, Y.-C.; Lee, J. W.; Soman, P.; Zorlutana, P.; Nichol, J. W.; Bae, H.; Chen, S.; Khademhosseini, A. Microfabrication of Complex Porous Tissue Engineering Scaffolds Using 3D Projection Stereolithography. *Biomaterials* **2012**, *33*, 3824−3834.
(5) Giannitelli, S. M.; Accoto, D.; Trombetta, M.; Rainer, A. Current Trends in the Design of Scaffolds for Computer-Aided Tissue Engineering. *Acta Biomater.* **2014**, *10*, 580−594.
(6) Sun, J.-Y.; Zhao, X.; Illeperuma, W. R. K.; Chaudhuri, O.; Oh, K. H.; Mooney, D. J.; Vlassak, J. J.; Suo, Z. Highly Stretchable and Tough Hydrogels. *Nature* **2012**, *489*, 133−136.
(7) Bhat, S.; Tripathi, A.; Kumar, A. Supermacroprous Chitosan−Agarose−Gelatin Cryogels: In Vitro Characterization and *In Vivo* Assessment for Cartilage Tissue Engineering. *J. R. Soc. Interface* **2011**, *8*, 540−554.
(8) Patnaik, S. S.; Wang, B.; Weed, B.; Wertheim, J. A.; Liao, J. In *Tissue Regeneration: Where Nanostructure Meets Biology*; Liu, Q.; Wang, H., Eds.; World Scientific Publishing Co Pte Ltd: Singapore, 2014; Chapter 3, pp 77−124.
(9) Badylak, S. F.; Taylor, D.; Uygun, K. Whole-Organ Tissue Engineering: Decellularization and Recellularization of Three-Dimensional Matrix Scaffolds. *Annu. Rev. Biomed. Eng.* **2011**, *13*, 27−53.
(10) Radisic, M.; Yang, L.; Boublik, J.; Cohen, R. J.; Langer, R.; Freed, L. E.; Vunjak-Novakovic, G. Medium Perfusion Enables Engineering of Compact and Contractile Cardiac Tissue. *Am. J. Physiol.: Heart Circ. Physiol.* **2004**, *286*, 507−516.
(11) Griffith, L. G.; Swartz, M. A. Capturing Complex 3D Tissue Physiology *In Vitro*. *Nat. Rev. Mol. Cell Biol.* **2006**, *7*, 211−224.
(12) Sampson, S. L.; Saravia, L.; Gustafsson, K.; Jayasinghe, S. N.; Robertson, B. D. Cell Electrospinning: An In Vitro and In Vivo Study. *Small* **2014**, *10*, 78−82.
(13) Hacker, M. C.; Mikos, A. G. Trends in Tissue Engineering Research. *Tissue Eng.* **2006**, *12*, 2049−2057.
(14) Sanz-Herrera, J. A.; Reina-Romo, E. Cell-Biomaterial Mechanical Interaction in the Framework of Tissue Engineering: Insights, Computational Modeling and Perspectives. *Int. J. Mol. Sci.* **2011**, *12*, 8217−8244.
(15) Lee, M. H.; Arcidiacono, J. A.; Bilek, A. M.; Wille, J. J.; Hamill, C. A.; Wonnacott, K. M.; Wells, M. A.; Oh, S. S. Considerations for Tissue-Engineered and Regenerative Medicine Product Development Prior to Clinical Trials in the United States. *Tissue Eng., Part B* **2010**, *16*, 41−54.
(16) O'Dea, R. D.; Osborne, J. M.; El Haj, A. J.; Byrne, H. M.; Waters, S. L. The Interplay between Tissue Growth and Scaffold Degradation in Engineered Tissue Constructs. *J. Math. Biol.* **2012**, *67*, 1199−1225.
(17) Kohane, D.; Langer, R. Biocompatibility and Drug Delivery Systems. *Chem. Sci.* **2010**, *1*, 441−446.
(18) Gonzalez-Simon, A. L.; Eniola-Adefeso, O. In *Engineering Biomaterials for Regenerative Medicine*; Bhatia, S. K., Ed.; Springer: NY, 2012; Chapter 6, pp 143−159.
(19) Place, E. S.; Evans, N. D.; Stevens, M. M. Complexity in Biomaterials for Tissue Engineering. *Nat. Mater.* **2009**, *8*, 457−470.
(20) Kim, T. G.; Shin, H.; Lim, D. W. Biomimetic Scaffolds for Tissue Engineering. *Adv. Funct. Mater.* **2012**, *22*, 2446−2468.
(21) Duron, A., Laurencin, C. T. In *Nanotechnology and Tissue Engineering: The Scaffold*; Laurencin, C. T., Nair, L. S., Eds.; CRC Press: Boca Raton, 2008; Chapter 6, pp 163−196.
(22) Romano, N. H.; Sengupta, D.; Chung, C.; Heilshorn, S. C. Protein-Engineered Biomaterials: Nanoscale Mimics of the Extracellular Matrix. *Biochim. Biophys. Acta* **2011**, *1810*, 339−349.
(23) Discher, D. E.; Janmey, P.; Wang, Y. Tissue Cells Feel and Respond to the Stiffness of Their Substrate. *Science* **2005**, *310*, 1139−1143.

(24) Brandl, F.; Sommer, F.; Goepferich, A. Rational Design of Hydrogels for Tissue Engineering: Impact of Physical Factors on Cell Behavior. *Biomaterials* **2007**, *28*, 134−146.
(25) Schlie-Wolter, S.; Ngezahayo, A.; Chichkov, B. N. The Selective Role of ECM Components on Cell Adhesion, Morphology, Proliferation and Communication *In Vitro*. *Exp. Cell Res.* **2013**, *319*, 1553−1561.
(26) Oh, S. H.; Kim, T. H.; Im, G. I.; Lee, J. H. Investigation of Pore Size Effect on Chondrogenic Differentiation of Adipose Stem Cells Using a Pore Size Gradient Scaffold. *Biomacromolecules* **2010**, *11*, 1948−1955.
(27) Lien, S. M.; Ko, L. Y.; Huang, T. J. Effect of Pore Size on ECM Secretion and Cell Growth in Gelatin Scaffold for Articular Cartilage Tissue Engineering. *Acta Biomater.* **2009**, *5*, 670−679.
(28) Oh, S. H.; Park, I. K.; Kim, J. M.; Lee, J. H. *In Vitro* and *in Vivo* Characteristics of PCL Scaffolds with Pore Size Gradient Fabricated by a Centrifugation Method. *Biomaterials* **2007**, *28*, 1664−1671.
(29) Harley, B. A.; Kim, H. D.; Zaman, M. H.; Yannas, I. V.; Lauffenburger, D. A.; Gibson, L. J. Microarchitecture of Three-Dimensional Scaffolds Influences Cell Migration Behavior via Junction Interactions. *Biophys. J.* **2008**, *95*, 4013−4024.
(30) Murphy, C. M.; Haugh, M. G.; O'Brien, F. J. The Effect of Mean Pore Size on Cell Attachment, Proliferation and Migration in Collagen-Glycosaminoglycan Scaffolds for Bone Tissue Engineering. *Biomaterials* **2010**, *31*, 461−466.
(31) Lee, M.; Wu, B. M.; Dunn, J. C. Y. Effect of Scaffold Architecture and Pore Size on Smooth Muscle Cell Growth. *J. Biomed. Mater. Res., Part A* **2008**, *87*, 1010−1016.
(32) Van Bael, S.; Chai, Y. C.; Truscello, S.; Moesen, M.; Kerckhofs, G.; Van Oosterwyck, H.; Kruth, J. P.; Schrooten, J. The Effect of Pore Geometry on the *In Vitro* Biological Behavior of Human Periosteum-Derived Cells Seeded on Selective Laser-melted Ti6Al4V Bone Scaffolds. *Acta Biomater.* **2012**, *8*, 2824−2834.
(33) Sobral, J. M.; Caridade, S. G.; Sousa, R. A.; Mano, J. F.; Reis, R. L. Three-Dimensional Plotted Scaffolds with Controlled Pore Size Gradients: Effect of Scaffold Geometry on Mechanical Performance and Cell Seeding Efficiency. *Acta Biomater.* **2011**, *7*, 1009−1018.
(34) Griffon, D. J.; Sedighi, M. R.; Schaeffer, D. V.; Eurell, J. A.; Johnson, A. L. Chitosan Scaffolds: Interconnective Pore Size and Cartilage Engineering. *Acta Biomater.* **2006**, *2*, 313−320.
(35) Hadjipanayi, E.; Mudera, V.; Brown, R. A. Close Dependence of Fibroblast Proliferation on Collagen Scaffold Matrix Stiffness. *J. Tissue Eng. Regener. Med.* **2009**, *3*, 77−84.
(36) Haugh, M. G.; Murphy, C. M.; McKiernan, R. C.; Altenbuchner, C.; O'Brien, F. J. Crosslinking and Mechanical Properties Significantly Influence Cell Attachment, Proliferation, and Migration Within Collagen Glycosaminoglycan Scaffolds. *Tissue Eng., Part A* **2011**, *17*, 1201−1208.
(37) Ghosh, K.; Pan, Z.; Guan, E.; Ge, S.; Liu, Y.; Nakamura, T.; Ren, X. D.; Rafailovich, M.; Clark, R. A. Cell Adaptation to a Physiologically Relevant ECM Mimic with Different Viscoelastic Properties. *Biomaterials* **2007**, *28*, 671−679.
(38) Chen, J.; Irianto, J.; Inamdar, S.; Pravincumar, P.; Lee, D. A.; Bader, D. L.; Knight, M. M. Cell Mechanics, Structure, and Function are Regulated by the Stiffness of the Three-Dimensional Microenvironment. *Biophys. J.* **2012**, *103*, 1188−1197.
(39) Saha, K.; Keung, A. J.; Irwin, E. F.; Li, Y.; Little, L.; Schaffer, D. V.; Healy, K. E. Substrate Modulus Directs Neural Stem Cell Behavior. *Biophys. J.* **2008**, *95*, 4426−4438.
(40) Reinhart-King, C. A.; Dembo, M.; Hammer, D. A. Cell-Cell Mechanical Communication Through Compliant Substrates. *Biophys. J.* **2008**, *95*, 6044−6051.
(41) Dikovsky, D.; Bianco-Peled, H.; Seliktar, D. Defining the Role of Matrix Compliance and Proteolysis in Three-Dimensional Cell Spreading and Remodeling. *Biophys. J.* **2008**, *94*, 2914−2925.
(42) Liu, C.; Abedian, R.; Meister, R.; Haasper, C.; Hurschler, C.; Krettek, C.; Lewinski, G. V.; Jagodzinski, M. Influence of Perfusion and Compression on the Proliferation and Differentiation of Bone Mesenchymal Stromal Cells Seeded on Polyurethane Scaffolds. *Biomaterials* **2012**, *33*, 1052−1064.
(43) Keselowsky, B. G.; Collard, D. M.; García, A. J. Integrin Binding Specificity Regulates Biomaterial Surface Chemistry Effects on Cell Differentiation. *Proc. Natl. Acad. Sci. U.S.A.* **2005**, *102*, 5953−5957.
(44) Koo, L. Y.; Irvine, D. J.; Mayes, A. M.; Lauffenburger, D. A.; Griffith, L. G. Co-Regulation of Cell Adhesion by Nanoscale RGD Organization and Mechanical Stimulus. *J. Cell Sci.* **2002**, *115*, 1423−1433.
(45) Brown, B. N.; Barnes, C. A.; Kasick, R. T.; Michel, R.; Gilbert, T. W.; Beer-Stolz, D.; Castner, D. G.; Ratner, B. D.; Badylak, S. F. Surface Characterization of Extracellular Matrix Scaffolds. *Biomaterials* **2010**, *31*, 428−437.
(46) Kisiday, J.; Jin, M.; Kurz, B.; Hung, H.; Semino, C.; Zhang, S.; Grodzinsky, A. J. Self-Assembling Peptide Hydrogel Fosters Chondrocyte Extracellular Matrix Production and Cell Division: Implications for Cartilage Tissue Repair. *Proc. Natl. Acad. Sci. U.S.A.* **2002**, *99*, 9996−10001.
(47) Ivirico, J. L.; Salmeron-Sanchez, M.; Ribelles, J. L.; Pradas, M. M.; Soria, J. M.; Gomes, M. E.; Reis, R. L.; Mano, J. F. Proliferation and Differentiation of Goat Bone Marrow Stromal Cells in 3D Scaffolds with Tunable Hydrophilicity. *J. Biomed. Mater. Res., Part B* **2009**, *91*, 277−286.
(48) Koh, H. S.; Yong, T.; Chan, C. K.; Ramakrishna, S. Enhancement of Neurite Outgrowth Using Nano-Structured Scaffolds Coupled with Laminin. *Biomaterials* **2008**, *29*, 3574−3582.
(49) Jithendra, P.; Rajam, A. M.; Kalaivani, T.; Mandal, A. B.; Rose, C. Preparation and Characterization of Aloe Vera Blended Collagen-Chitosan Composite Scaffold for Tissue Engineering Applications. *ACS Appl. Mater. Interfaces* **2013**, *5*, 7291−7298.
(50) Santos, E.; Hernández, R. M.; Pedraz, J. L.; Orive, G. Novel Advances in the Design of Three-Dimensional Bio-Scaffolds to Control Cell Fate: Translation from 2D to 3D. *Trends Biotechnol.* **2012**, *30*, 331−341.
(51) Williams, D. F. On the Mechanisms of Biocompatibility. *Biomaterials* **2008**, *29*, 2941−2953.
(52) Gornall, J. L.; Terentjev, E. M. Universal Kinetics of Helix-Coil Transition in Gelatin. *Phys. Rev. E: Stat., Nonlinear, Soft Matter Phys.* **2008**, *77*, 031908.
(53) Mckinney, R. M.; Spillane, J. T.; Pearce, G. W. Factors Affecting the Rate of Reaction of Fluorescein Isothiocyanate with Serum Proteins. *J. Immunol.* **1964**, *93*, 232−242.
(54) Griffith, O. H.; McConnell, H. M. A Nitroxide-Maleimide Spin Label. *Proc. Natl. Acad. Sci. U.S.A.* **1966**, *55*, 8−11.
(55) Plieva, F. M.; Kumar, A.; Galaev, I. Y.; Mattiasson, B. In *Advanced Biomaterials*; Basu, B., Katti, D. S., Kumar, A., Eds.; John Wiley & Sons, Inc.: New Jersey, 2010; Chapter 14, pp 499−531.
(56) Klare, J. P.; Steinhoff, H.-J. Spin Labelling EPR. *Photosynth. Res.* **2009**, *102*, 377−390.
(57) Nesmelov, Y. E.; Thomas, D. D. Protein Structural Dynamics Revealed by Site-Directed Spin Labeling and Multifrequency EPR. *Biophys. Rev.* **2010**, *2*, 91−99.
(58) Štrancar, J. In *ESR Spectroscopy in Membrane Biophysics*; Hemminga, M. A., Berliner, L. J., Eds.; Springer Science: New York, 2007; Chapter 3, pp 49−93.
(59) Stopar, D.; Štrancar, J.; Spruijt, R. B.; Hemminga, M. A. Motional Restrictions of Membrane Proteins: A Site-Directed Spin Labeling Study. *Biophy. J.* **2006**, *91*, 3341−3348.
(60) Štrancar, J.; Kavalenka, A.; Urbančič, I.; Ljubetič, A.; Hemminga, M. A. SDSL-ESR-Based Protein Structure Characterization. *Eur. Biophys. J.* **2010**, *39*, 499−511.
(61) Kavalenka, A.; Urbančič, I.; Belle, V.; Rouger, S.; Constanzo, S.; Kure, S.; Fournel, A.; Longhi, S.; Guigliarelli, B.; Štrancar, J. Conformational Analysis of the Partially Disordered Measles Virus NTAIL-XD Complex by SDSL EPR Spectroscopy. *Biophys. J.* **2010**, *98*, 1055−1064.
(62) Schmidt, A.; Gaul, L. In *Proceedings of the International Model Analysis Conference*; Society for Experimental Mechanics, Bethel, 2008; Vol. 3, pp 1557−1566.

(63) Banks, H. T.; Hu, S.; Kenz, Z. R. A Brief Review of Elasticity and Viscoelasticity for Solids. *J. Appl. Math. Mech.* **2011**, *3*, 1−51.
(64) Page, B.; Page, M.; Noel, C. A New Fluorometric Assay for Cytotoxicity Measurements In-Vitro. *Int. J. Oncol.* **1993**, *3*, 473−476.
(65) Sengers, B. G.; Taylor, M.; Please, C. P.; Oreffo, R. O. C. Computational Modelling of Cell Spreading and Tissue Regeneration in Porous Scaffolds. *Biomaterials* **2007**, *28*, 1926−1940.
(66) Sung, H. J.; Meredith, C.; Johnson, C.; Galis, Z. S. The Effect of Scaffold Degradation Rate on Three-Dimensional Cell Growth and Angiogenesis. *Biomaterials* **2004**, *25*, 5735−5742.
(67) Karamichos, D.; Brown, R. A.; Mudera, V. Collagen Stiffness Regulates Cellular Contraction and Matrix Remodeling Gene Expression. *J. Biomed. Mater. Res., Part A* **2007**, *83*, 887−894.